Not Just Par for the Course: 73 Quaternary Germanides RE_4M_2XGe$_4$ (RE = La–Nd, Sm, Gd–Tm, Lu; M = Mn–Ni; X = Ag, Cd) and the Search for Intermetallics with Low Thermal Conductivity

Dong Zhang,[†] Anton O. Oliynyk,[†,*] Gabriel M. Duarte,[†] Abishek K. Iyer,[†] Leila Ghadbeigi,[‡] Steven K. Kauwe,[‡] Taylor D. Sparks,[‡,*] and Arthur Mar[†,*]

[†] *Department of Chemistry, University of Alberta, Edmonton, Alberta, Canada T6G 2G2*

[‡] *Department of Materials Science and Engineering, University of Utah, Salt Lake City, UT, USA 84112*

Abstract

A total of 73 new quaternary rare-earth germanides RE_4M_2XGe$_4$ (RE = rare-earth metal; M = Mn–Ni; X = Ag, Cd) were prepared through reactions of the elements. The solid solution Nd$_4$Mn$_2$Cd(Ge$_{1-y}$Si$_y$)$_4$ was also prepared under the same conditions and was found to be complete over the entire range. All of these compounds adopt the monoclinic Ho$_4$Ni$_2$InGe$_4$-type structure (space group $C2/m$, a = 14.2–16.7 Å, b = 4.0–4.6 Å, c = 6.8–7.5 Å, β = 106–109°), as revealed by powder X-ray diffraction analysis, as well as single-crystal X-ray diffraction analysis on selected members. The structure determination of Nd$_4$(Mn$_{0.78(1)}$Ag$_{0.22(1)}$)$_2$Ag$_{0.83(1)}$Ge$_4$ disclosed disorder of Mn and Ag atoms within the tetrahedral site and Ag deficiencies within the square planar site. Within the solid solution Nd$_4$Mn$_2$Cd(Ge$_{1-y}$Si$_y$)$_4$, the end-members and two intermediate members were structurally characterized; as the Si content increases, the Cd sites become less deficient and the individual [Mn$_2$$Tt_2$] layers contract but become further apart from each other. Electronic band structure calculations confirm that the Ag–Ge or Cd–Ge bonds are the weakest in the structure and thus prone to distortion. Thermal property measurements confirm expectations from machine-learning predictions that these quaternary germanides should exhibit low thermal conductivity, which was found to be <10 W m^{-1} K^{-1} for Nd$_4$Mn$_2$AgGe$_4$.

Keywords: Rare-earth intermetallics; Germanides; Solid solution; Crystal structure; Electronic structure; Thermal properties

Introduction

Intermetallic germanides exhibit a rich structural chemistry having many similarities to silicides, but with a more pronounced tendency for dense and complex atomic arrangements that reflect the greater metallic character of the bonding. They are especially plentiful in combination with rare-earth metals.[1] Many ternary rare-earth germanides *RE*–*M*–Ge (where *M* is a d-block metal or p-block metalloid) show interesting physical properties such as superconductivity (e.g., YM_2Ge$_2$, RE_2Ir$_3$Ge$_5$)[2–4] and magnetocaloric effects (e.g., Gd$_5$Si$_2$Ge$_2$).[5] The number of quaternary rare-earth germanides *RE*–*M*–*M*′–Ge is potentially very large, with several thousand possible combinations of elements, but only a few hundred compounds have been identified so far.[6] Many previously known quaternary germanides, such as *RE*AuAl$_4$Ge$_2$,[7] RE_3CoAl$_3$Ge$_2$,[8] *REM*Ga$_3$Ge (*M* = Co, Ni),[9] RE_2MGa$_9$Ge$_2$ (*M* = Co, Ni),[10] Yb$_7$Ni$_4$InGe$_{12}$,[11] and Yb$_3$AuIn$_3$Ge$_2$,[12] were inadvertently obtained in the presence of Al, Ga, or In reactive fluxes. Site disorder of metal components is frequently observed in the structures of these quaternary germanides. However, an ordered arrangement of all four elements is found in the versatile Ho$_4$Ni$_2$InGe$_4$-type structure.[13] Through systematic investigations, we have recently expanded the number of representatives in this structure type so that it is currently the most prevalent among quaternary rare-earth germanides known to date. About 60 compounds RE_4M_2InGe$_4$ (*M* = Mn, Fe, Co, Ni, Ru, Rh, Ir) were synthesized,[14,15] and they were established to be thermodynamically stable phases that do not require a flux to be prepared.[16] Moreover, the analysis of this quaternary structure type in terms of cutting strips out of a parent ternary germanide RE_2InGe$_2$ led to the derivation of a different quaternary germanide RE_4RhInGe$_4$.[15,17]

In general, the metallic behaviour of intermetallic compounds renders them unfavourable for applications such as good thermoelectric materials unless they fall into a special category in

which a hybridization gap forms.[18–21] Identifying new intermetallic compounds which exhibit inherent structural features that give rise to low thermal conductivity is thus important in gaining insight for designing thermoelectric materials. We have been interested in applying machine-learning approaches to discover intermetallic compounds with specific structures and properties.[22,23] These methods show promise in aiding the accelerated search for new materials and guiding synthetic efforts by suggesting candidates different from existing ones. These models are built by applying various algorithms (e.g., support vector machine, random forest) to relate experimental crystal data and physical property measurements to chemical descriptors, enabling predictions of new materials to be made. In particular, machine-learning models have been developed to recommend new candidates for thermoelectric materials and to predict relevant properties such as thermal conductivity and heat capacity.[24–27] Although machine learning has become exceedingly popular for predicting new materials, experimental validation of these models remains sparse.[28–33]

In this study, we address further questions engendered by the previous work on $RE_4M_2InGe_4$ and by the desire to apply machine-learning methods to identify novel candidates for thermoelectric materials. First, given that the substitutional ranges for *RE* and *M* components are quite broad, would the same versatility be extended to substitution for the In and Ge components to expand the scope of these quaternary germanides to $RE_4M_2XTt_4$? Thus, we explore the possibility that In can be substituted by neighbouring d-block elements (*X* = Ag, Cd), and Ge by a lighter tetrel (*Tt* = Si). These changes are more drastic and are expected to be more difficult than the previous substitutions of *RE* and *M* components. In particular, it is not obvious if the unusual feature of square planar coordination of Ge atoms around the In centres observed in $RE_4M_2InGe_4$ can be retained by substitutions of these components. Second, and perhaps more

bold, does the encapsulation of the square planar centre within a large cage in the structure lead to atomic rattling, thereby enhancing the possibility of obtaining low thermal conductivity within an intermetallic compound? These germanides serve as a fascinating test case to validate the machine-learning models for predicting thermal conductivities and heat capacities of inorganic solids.

Experimental Section

Synthesis. Starting materials were freshly filed pieces of normally trivalent rare-earth metals (*RE* = La–Nd, Sm, Gd–Tm, Lu; 99.9%, Hefa), powders of transition metals (*M* = Mn, Fe, Co, Ni; >99%, Cerac or Alfa; and *X* = Ag, Cd; 99.95%, Alfa or Mackay), and elemental Ge (powder, 99.999%, Aldrich; or ingot, 99.9999%, Alfa). Mixtures of the components in the stoichiometric ratio of *RE*:*M*:*X*:Ge = 4:2:1:4 with a total mass of 0.20 g were pressed into pellets. The Ag-containing samples were arc-melted twice in a Centorr 5TA tri-arc furnace on a water-cooled copper hearth under an argon atmosphere. The mass loss of all arc-melted samples was less than 5%, and for most samples, it was less than 1%. Arc-melting of the Cd-containing samples was not attempted because the high vapour pressure of Cd would be anticipated to cause difficulties in maintaining the correct stoichiometry. The arc-melted ingots of the Ag-containing samples and the cold-pressed pellets of the Cd-containing samples were then placed in fused-silica tubes, which were evacuated and sealed. The tubes were heated at 800 °C for 10 d, after which they were quenched in cold water for the Ag-containing samples or allowed to cool to room temperature for the Cd-containing samples.

Formation of the solid solution $Nd_4Mn_2Cd(Ge_{1-y}Si_y)_4$ was investigated. In addition to the end-member $Nd_4Mn_2CdGe_4$ already obtained as described above, additional Si-containing

samples were prepared with nominal compositions $Nd_4Mn_2CdGe_2Si_2$, $Nd_4Mn_2CdGe_{1.5}Si_{2.5}$, and $Nd_4Mn_2CdSi_4$. Si powder (>99%, Alfa) was combined with the other elements, the mixtures were cold-pressed into pellets and placed into evacuated fused-silica tubes, and the same heat treatment at 800 °C was used as before.

Powder X-ray diffraction (XRD) patterns of the ground samples were collected on an Inel diffractometer equipped with a curved position-sensitive detector (CPS 120) and a Cu $K\alpha_1$ radiation source operated at 40 kV and 20 mA. The patterns were analyzed with the CSD suite of programs.[34] Table S1 in Supporting Information lists the phases and their relative amounts (estimated from peak heights) obtained in the samples. Table 1 summarizes the results and identifies which reactions were successful in forming the quaternary germanides, and Table 2 lists their cell parameters refined from the powder XRD data. Energy-dispersive X-ray (EDX) analysis was carried out on a JEOL JSM-6010LA InTouchScope scanning electron microscope operated with an accelerating voltage of 20 kV and acquisition times of 70 s, to determine the compositions of selected crystals or establish the phase equilibria of polished samples.

Structure Determination. Suitable single crystals of the quaternary germanides were difficult to extract from the samples prepared above because they tended to be small (typically less than 10 μm in their longest dimension) and irregularly shaped. Considerable effort was expended to select crystals from the Nd-containing samples because these compounds were eventually used for property measurements and for investigating the solid solubility with Si. Representative single crystals were selected from the $Nd_2Mn_2AgGe_4$ ingots and $Nd_2Mn_2Cd(Ge_{1-y}Si_y)_4$ bulk samples. Intensity data were collected at room temperature on a Bruker PLATFORM diffractometer equipped with a SMART APEX II CCD detector and a graphite-monochromated Mo $K\alpha$ radiation source, using ω scans at 6–8 different ϕ angles with a frame width of 0.3º and

an exposure time of 12 s per frame. Face-indexed numerical absorption corrections were applied. Structure solution and refinement were carried out with use of the SHELXTL (version 6.12) program package.[35] The monoclinic centrosymmetric space group *C*2/*m* was chosen on the basis of Laue symmetry and intensity statistics, and direct methods confirmed models in agreement with the expected $Ho_4Ni_2InGe_4$-type structure.[13] Atomic positions and labels were standardized with the program STRUCTURE TIDY.[36]

The main challenges in the structure determinations related to the treatment of partial occupancy and site disorder. Because substoichiometry on the square planar In site has been observed in many previously known $RE_4M_2InGe_4$ compounds,[14,15] this possibility was also considered for the analogous Ag and Cd sites in $Nd_2Mn_2AgGe_4$ and $Nd_2Mn_2Cd(Ge_{1-y}Si_y)_4$. When the occupancies of these sites were refined, they converged to values of 0.83(1) Ag in $Nd_4Mn_2AgGe_4$ and 0.86(1)–0.97(3) Cd in $Nd_2Mn_2Cd(Ge_{1-x}Si_x)_4$. We assume that the square planar site is occupied strictly by Ag or Cd atoms, and undergoes no mixing with Mn atoms, because the distances to the surrounding Ge atoms (3.0 Å or longer) would be far too long for Mn–Ge bonds. The remaining sites in these structures are generally well behaved and were found to be fully occupied. However, in the case of $Nd_4Mn_2AgGe_4$, the displacement parameters for the tetrahedral Mn site were anomalous low (U_{eq} = 0.0034(4) Å^2) compared to those for the other sites (U_{eq} = 0.0116(2)–0.0197(7) Å^2). A possible explanation is that this site contains a disordered mixture of Mn and Ag atoms. When such a model was refined, the occupancies converged to 0.78(1) Mn and 0.22(1) Ag, the displacement parameters became more reasonable (U_{eq} = 0.0116(4) Å^2), and the agreement factors improved slightly (conventional $R(F)$ decreasing from 0.043 to 0.038).

For different members of the $Nd_4Mn_2Cd(Ge_{1-y}Si_y)_4$ solid solution, the two available tetrel (group-14 element, *Tt* = Si, Ge) sites were allowed to be fully occupied with a mixture of Si and Ge atoms, with no constraints placed on the overall composition. The refined compositions agreed well with the nominal compositions. In two of the structure determinations, the checkCIF reports gave alerts detected by the TwinRotMat algorithm in PLATON that twinning may be present.[37] When the suggested twin laws were applied, the BASF values converged to 0.016(2) or 0.047(3) in $Nd_4Mn_2CdGe_4$ and $Nd_4Mn_2CdGe_{1.5}Si_{2.5}$, respectively, with the conventional *R*(*F*) values showing a small improvement.

Tables S2–S4 in Supporting Information lists full crystallographic data. Table 3 lists abbreviated crystallographic data and Table 4 lists ranges of interatomic distances.

Band Structure Calculations. Tight-binding linear muffin tin orbital band structure calculations were performed for fully stoichiometric and ordered models for $La_4Mn_2AgGe_4$ and $La_4Mn_2CdGe_4$ within the local density and atomic spheres approximation with use of the Stuttgart TB-LMTO-ASA program (version 4.7).[38] The basis sets consisted of La 6s/6p/5d/4f, Mn 4s/4p/3d, Ag or Cd 5s/5p/4d/4f, and Ge 4s/4p/4d orbitals, with the La 6p/4f, Ag or Cd 4f, and Ge 4d orbitals being downfolded. Integrations in reciprocal space were carried out with an improved tetrahedron method over 132 irreducible *k* points within the first Brillouin zone. Bonding characteristics were evaluated through an energy-resolved visualization as quantified by crystal orbital Hamilton populations (COHP).[39]

Machine-Learning Predictions. Within a thermoelectrics recommendation engine developed previously and available online,[25] any arbitrary chemical formula can be entered and the probability that such a composition will exhibit a thermal conductivity lower than 10 W m^{-1} K^{-1} can be computed. Various members of $RE_4M_2XGe_4$ were evaluated in this manner, revealing

probabilities greater than 95% for all of them. Similarly, a machine-learning model for predicting heat capacities solely from a chemical formula was previously developed by us based on a training set of thermochemical data obtained from NIST:JANAF tables.[27] The heat capacity of $Nd_4Mn_2InGe_4$ and $Nd_4Mn_2AgGe_4$ was predicted using this model at various temperatures.

Thermal Conductivity. Samples of the previously known compound $Nd_4Mn_2InGe_4$ [14] and the new compound $Nd_4Mn_2AgGe_4$ were available in the form of annealed arc-melted ingots. These Nd-containing samples were chosen for measurement based on the earlier success in preparing $Nd_4Mn_2InGe_4$ in high purity and large quantities. The thermal conductivities κ of these samples were determined from the standard relationship $\kappa = \rho\alpha C_p$, where ρ is the density, α is the thermal diffusivity, and C_p is the heat capacity at constant pressure. The ingots do not show any large pores and based on similar types of samples measured previously, their density was estimated to be no less than 95% of that calculated from the single-crystal diffraction data. The thermal diffusivity was measured using the laser flash method with a Netzsch LFA 457 instrument with a Cape-Lehman pulse length and heat loss correction model.[40] The samples were polished to become coplanar with a thickness of 3 mm, cut into disc shapes with 8–12 mm diameter via electrical discharge machining, and then coated with graphite on both sides to promote uniform absorption and emission. Measurements were taken from room temperature to 600 °C in increments of 100 °C. Heat capacity values were obtained from high accuracy predictions [27] and verified on a Perkin Elmer Pyris 1 DSC instrument. The samples were small fragments cut from the ingots. Calorimetry measurements were taken from 200 to 600 °C.

Results and Discussion

Phase Analysis. Given the existence of the quaternary In-containing germanides $RE_4M_2InGe_4$,[13–15] synthetic investigations were focused on replacing In with either Ag or Cd. The targeted compounds belong to 8 series $RE_4M_2XGe_4$ (M = Mn, Fe, Co, Ni; X = Ag, Cd), with the RE components being limited to 12 normally trivalent members (RE = La–Nd, Sm, Gd–Tm, Lu). In total, 96 samples were prepared through reactions of the elements at 800 °C for 10 d, with a preliminary arc-melting step applied to the Ag-containing samples. Out of these samples, 73 contained the desired quaternary phase (Table 1). Multiphase samples were the norm, with the quaternary compound typically being accompanied by two or three other phases (Table S1 in Supporting Information). Some samples contained small amounts of oxide impurities, possibly as a result of brief exposure to air during the transfer of the arc-melted ingots to fused-silica tubes. Oxide phases within some of the Ni-containing samples in $RE_4Ni_2CdGe_4$ series were eventually traced to impurities within the Ni metal source used. In a few favourable cases, nearly phase-pure samples were obtained, as indicated by powder XRD patterns and backscattered SEM images on representative samples (Figure S1 in Supporting Information). To be sure, optimizing the preparation of phase-pure samples will depend on a case-by-case basis for individual compounds. As detailed below, there is evidence that these compounds are substoichiometric. Maintaining a specific composition is also tricky because of volatilization losses of elements such as Cd, which are difficult to control. However, pressing the components into pellets before arc-melting helps minimize these volatilization losses.

The powder XRD patterns for all quaternary germanides $RE_4M_2XGe_4$ (X = Ag, Cd) prepared here were fit to monoclinic unit cells, with refined parameters listed in Table 2. Plots of the unit cell volumes as a function of RE generally show the expected decrease due to the lanthanide contraction (Figure 1). However, the trends are not as regular as in the previously

reported In-containing series $RE_4M_2InGe_4$,[13–15] likely because the compounds show substantial variability in the levels of Ag or Cd deficiencies (x in the substoichiometric compositions $RE_4M_2X_{1-x}Ge_4$). The existence of these deficiencies was confirmed in selected compounds examined with single-crystal X-ray diffraction, as described later. In fact, the trends are quite irregular for the Ag-containing series, consistent with the tendency of Ag to exhibit such deficiencies in many of its compounds. On progressing along different series varying with *M*, the cell volumes generally decrease, following the trend in atomic sizes from Mn to Ni; the range of *RE* substitution also becomes more restricted so that the Ni-containing series forms only for the mid-lanthanides. These observations suggest that size factors limit the formation of these quaternary germanides. A plot of radius ratios r_M/r_X and r_{RE}/r_X, where Pauling metallic radii R_1 were taken to evaluate these ratios,[41] supports this proposal (Figure 2), although the regions of formation differ for the Ag- vs. Cd-containing series. It should be possible to prepare the analogous germanides with the *M* component being substituted by heavier congeners (e.g., Ru, Rh, Ir), which would be predicted to be compatible with larger *RE* components.

Structure of $RE_4M_2XGe_4$. The crystal structures of $Nd_4Mn_2AgGe_4$ and $Nd_4Mn_2CdGe_4$, selected as representative examples of $RE_4M_2XGe_4$, were determined from single-crystal X-ray diffraction data, and confirmed to be the monoclinic $Ho_4Ni_2InGe_4$-type structure.[13] This structure has been described in detail previously, including its relationships to ternary structures,[15] and we review here the salient features. This versatile structure, which is remarkable for exhibiting well-ordered sites within a quaternary intermetallic compound, can be viewed in different ways (Figure 3). It can be derived by cutting slabs from the tetragonal Mo_2FeB_2-type structure (which is adopted by many ternary germanides, such as RE_2CdGe_2 and RE_2InGe_2, and is built up of a stacking of 3^2434 nets) and shifting these slabs relative to each

other.[14,15,17,42] This viewpoint highlights the presence of Ge-centred trigonal prisms, which are commonly found in many intermetallic germanides, and *X*-centred tetragonal prisms. Alternatively, the structure can be regarded in terms of cationic *RE* atoms embedded within the tunnels of an anionic [M_2XGe$_4$] framework, which is built up of ladders of edge-sharing MGe$_4$ tetrahedra extending along the *b*-direction and XGe$_4$ square planes. Adjacent ladders are linked together via Ge$_2$ pairs (yellow bonds) to form infinite layers [M_2Ge$_4$] lying parallel to (001), and these layers in turn are connected through the *X* atoms. The coordination environment of 4 Ge and 8 *RE* atoms around the *X* atoms also generates a cuboctahedron, which share opposite square faces with neighbouring cuboctahedra to form a stack along the *b*-direction.

The structures of RE_4M_2XGe$_4$ are susceptible to additional complications. First, these compounds are definitely substoichiometric in *X*, as seen in Nd$_4$Mn$_2$Cd$_{0.86(1)}$Ge$_4$, but the level of deficiency is more pronounced than in the In-containing series (RE_4M_2In$_{0.93(2)–0.99(2)}$Ge$_4$).[14,15] The substoichiometry persists in the solid solutions with Si, as described below. Although further structure determinations are desirable, the persistent observation of the substoichiometry in the *X* site suggests that it is an inherent feature in all RE_4M_2XGe$_4$ compounds. Second, the *M* and *X* atoms may be disordered. The square planar coordination geometry of Ag or Cd atoms is certainly unusual, but it is not unprecedented.[43] Nevertheless, it is possible that such atoms may also occupy the tetrahedral sites. The structure determination of Nd$_4$Mn$_2$AgGe$_4$ reveals that not only do Ag atoms reside within the larger square planar site (with an occupancy of 0.83(1) Ag and distances of 2.958(1)–3.166(2) Å to surrounding Ge atoms), but they also mix with the Mn atoms within the smaller tetrahedral site (with occupancies of 0.78(1) Mn and 0.22(1) Ag, and distances of 2.621(1)–2.692(2) Å to surrounding Ge atoms). This phenomenon can be rationalized by the propensity of Ag to exhibit quite variable bond lengths; specifically, Ag–Ge

bonds can range widely from 2.4 to 3.0 Å.[44] With both site deficiency and site disorder occurring, the resulting formula for this compound is $Nd_4Mn_{1.55(2)}Ag_{1.25(2)}Ge_4$, although for simplicity, we will continue to use the ideal formula $RE_4M_2X Ge_4$ in subsequent discussion.

Disorder of Ge and Si. Silicides and germanides share many similarities, but it is not a truism that they always form isostructural compounds. In fact, solid solutions of silicides and germanides are not as common as one thinks.[45,46] To explore whether Si can substitute for Ge within the quaternary germanides $RE_4M_2X Ge_4$, the mixed system $Nd_4Mn_2Cd(Ge_{1-y}Si_y)_4$ was chosen for investigation. Two intermediate members with nominal compositions $Nd_4Mn_2CdGe_2Si_2$ and $Nd_4Mn_2CdGe_{1.5}Si_{2.5}$, as well as the silicide $Nd_4Mn_2CdSi_4$ were targeted, using the same preparative conditions as before. The desired compounds were obtained and single-crystal structure determinations confirmed that they adopt the monoclinic $Ho_4Ni_2InGe_4$-type structure as well. As in the parent germanides, all members examined in this solid solution also exhibit substoichiometry in the *X* site, so the formulas should strictly be written as $Nd_4Mn_2Cd_{1-x}(Ge_{1-y}Si_y)_4$. As the Si content is increased in $Nd_4Mn_2Cd(Ge_{1-y}Si_y)_4$, the structure evolves in an interesting way (Figure 4). Vegard's law is not followed, with the cell parameters for the intermediate members being greater than those for the end members. The unit cell volume first expands on progressing from $Nd_4Mn_2CdGe_4$ to $Nd_4Mn_2CdGe_2Si_2$, counter to expectations, and then contracts on progressing further to $Nd_4Mn_2CdSi_4$. Preferential site occupation is a typical reason for deviations from Vegard's law.[47] However, the refined occupancies of Ge and Si atoms within the two tetrel sites in the structure, *Tt*1 and *Tt*2, are close to the nominal compositions and vary nearly linearly with the loaded Si content. The gradual increase in the occupancy of the Cd site, from 0.86(1) in the all-Ge member to 0.97(1) in the all-Si member, may contribute to the expansion in the unit cell. The most compelling observation,

however, comes from inspecting key interatomic distances in the structures. As smaller Si atoms are introduced in place of Ge atoms, the bonds within the *Tt*1–*Tt*1 pairs in the structure shorten, as do the average Mn–*Tt* distances within the Mn-centred tetrahedra, but to a lesser extent. In contrast, the Cd–*Tt* distances within the Cd-centred square planes lengthen. In an analysis of the previous In-containing series $RE_4M_2InGe_4$, we had proposed that the bonds within the $InGe_4$ square planes are weak and highly susceptible to distortion.[15] In a similar way, within the solid solution $Nd_4Mn_2Cd(Ge_{1-y}Si_y)_4$, it is important to satisfy the requirements of the stronger Mn–*Tt* and *Tt*–*Tt* bonds foremost, at the expense of the weaker Cd–*Tt* bonds. That is, as Si substitutes for Ge atoms, there is a contraction of the individual [M_2Tt_2] layers that lie parallel to (001), but this effect is counteracted by an expansion accompanying the greater separation of these layers.

Electronic Structure. To examine the bonding in more detail in these new quaternary germanides and to draw comparisons to the previous In-containing compounds, non-spin-polarized electronic band structure calculations were carried out on idealized stoichiometric, ordered models of $La_4Mn_2AgGe_4$ and $La_4Mn_2CdGe_4$. These La-containing members were chosen to avoid complications associated with partially occupied 4f orbitals. The density of states (DOS) and crystal orbital Hamilton population (COHP) curves are shown in Figure 5. The Fermi level lies within a broad manifold (from around –4 eV upwards in energy) characterized by significant mixing of Mn 3d, Ag or Cd 5s/5p, and Ge 4p states. The position of the Fermi level near a local maximum composed primarily of Mn 3d states suggests that, at least for these Mn-containing compounds, magnetic ordering is likely. Most of the La-based states lie well above the Fermi level, but they do contribute to the DOS below, especially around –2 eV. The 4d states of the Ag or Cd atoms are much more localized and completely filled within the narrow sharp spikes in the DOS, which lie quite deep in energy below the Fermi level at –4.3 or – 8.8

eV, respectively, so they cannot influence the electrical properties significantly. Moreover, these 4d states participate little in bonding to the surrounding Ge atoms, as seen in the Ag–Ge or Cd–Ge COHP curves. Although many of the features of the electronic structures within the series $La_4Mn_2AgGe_4$, $La_4Mn_2CdGe_4$, and $La_4Mn_2InGe_4$ are similar, it is not a simple matter of raising the Fermi level by increasing the electron count, as a rigid band approximation would imply. As seen in the COHP curves and quantified by the integrated COHP values (Table 5), the Mn–Ge and Ge–Ge bonds are inherently the strongest ones within the structure and it is important to optimize them by ensuring that all bonding levels are occupied. In contrast, the Ag–Ge or Cd–Ge bonds are the weakest, corroborating the description above of how the structure can evolve by allowing these bonds to distort. Near the Fermi level, the Mn–Ge, Ag–Ge or Cd–Ge, and Ge–Ge interactions are nonbonding or only weakly antibonding. Depopulation of these levels (counterbalanced by the weakening of La–Ge bonding) thus provides a possible rationalization for why deficiencies readily occur in these compounds.

Thermal Conductivity. Intermetallic compounds typically exhibit high thermal conductivities (on the order of 10^2 W m^{-1} K^{-1}), which make them useful in applications such as high-temperature structural materials in which heat must be efficiently transferred.[48] On the other hand, this very characteristic normally rules them out as viable thermoelectric materials, which require low thermal conductivities. Although experimental measurements of thermal properties of intermetallics remain quite limited, the general trends are that the thermal conductivity tends to decrease with greater chemical complexity, deviations from ideal stoichiometry, and occurrence of disorder and defects, all of which are exhibited by these quaternary germanides RE_4M_2XGe$_4$. In a separate approach, machine-learning models have been recently developed for thermal conductivities and temperature-dependent heat capacities of

inorganic solids.[24–27] With use of a random forest algorithm and an experimental data set of known materials, a thermoelectrics recommendation engine was built in which, among various properties, the thermal conductivity of new materials could be predicted solely based on their composition;[25] in particular, using these tools, we were able to predict with high confidence (>95% probability) that any of these quaternary germanides would exhibit thermal conductivities lower than 10 W m^{-1} K^{-1}, so it is of interest to test these predictions. Because $Nd_4Mn_2InGe_4$ and $Nd_4Mn_2AgGe_4$ could be prepared in high purity, thermal measurements were made on these samples (Figure 6). The thermal conductivity was evaluated from temperature-dependent measurements of the thermal diffusivity and heat capacity through the relationship $\kappa = \rho\alpha C_p$. At elevated temperatures, the heat capacities of the samples are very nearly equal to the Dulong-Petit limits of 3*R* (0.251 J g^{-1} K^{-1} for $Nd_4Mn_2InGe_4$ and 0.253 J g^{-1} K^{-1} for $Nd_4Mn_2AgGe_4$). The baselines shown for the temperature-dependent heat capacities are predicted from machine learning [27] and the data points come from experimental measurements. Given the error and difficulty in measuring heat capacity, it has become common practice to simply use the 3*R* approximation over all temperatures when calculating the temperature-dependent thermal conductivity. On the other hand, in a recent work by Kauwe et al.,[27] it was shown that machine-learning predictions of heat capacity introduce significantly less error than the Dulong-Petit approximation as well as standard approaches such as Neumann-Kopp or cation/anion constituents calculations of heat capacity. In fact, the error of machine-learning predictions was less than 10% over all temperature ranges modeled, suggesting that it is on par with experimental determinations. Although the temperature dependence of the machine-learning results and experimental measurements may appear to be contrasting, they are within experimental error of each other. To calculate the thermal conductivities below 200 °C, the baseline values for heat

capacity were used. As the temperature increases from 100 °C to 600 °C, the thermal conductivity gradually increases from 3.5 W m^{-1} K^{-1} to reach a plateau of about 7 W m^{-1} K^{-1} for both compounds.

Conclusions

The number of quaternary germanides RE_4M_2XGe$_4$ adopting the ordered $Ho_4Ni_2InGe_4$-type structure has been more than doubled through the substitution of the *X* component, previously limited to In, with the late d-block elements Ag and Cd. Moreover, the elucidation of the complete solid solution $Nd_2Mn_2Cd(Ge_{1-x}Si_x)_4$ indicates that the corresponding quaternary silicides can be prepared. These results fulfill expectations that the $Ho_4Ni_2InGe_4$-type can accommodate considerable compositional versatility, which remains to be fully realized. Some of the key insights gained from the structural study of these germanides are that deficiencies in square planar *X* site persist and in fact, become more pronounced in the Ag- and Cd-containing members; that disorder of the *M* and *X* atoms within the tetrahedral site may occur if size factors permit, as observed in $Nd_4Mn_{1.55(2)}Ag_{1.25(2)}Ge_4$ (which could also be represented as $Nd_4(Mn_{0.78(1)}Ag_{0.22(1)})_2Ag_{0.83(1)}Ge_4$); and that maintenance of strong *M*–*Tt* and *Tt*–*Tt* bonding within [M_2Tt_2] layers, at the expense of weak *X*–*Tt* bonding within the square planes, is an important driving force in the evolution of the solid solution $Nd_4Mn_2Cd(Ge_{1-y}Si_y)_4$. The hypothesis that atomic rattling may be occuring within the square planar *X* sites is not fulfilled: the displacement parameters of the *X* atoms are not overwhemingly larger than those of the other sites. Nevertheless, electronic structure calculations indicate that the bonds to these *X* atoms are the weakest in the structure, which accounts for their flexibility. Low thermal conductivities were observed in $Nd_4Mn_2InGe_4$ and $Nd_4Mn_2AgGe_4$, in agreement with predictions from a

machine-learning model, but this behaviour may originate not only from the large cage-like geometry around the *X* atoms, but also from the complexity of the structure and the occurrence of defects and disorder. The next steps in this investigation would be to optimize synthetic conditions of these germanides to improve crystal growth so that further single-crystal structures can be determined to verify that the substoichiometry in the *X* site is a general phenomenon, and to obtain pure phases for confirming predictions that low thermal conductivity should be observed in other $RE_4M_2X\mathrm{Ge}_4$ members.

Table 1. Formation of Quaternary Germanides $RE_4M_2AgGe_4$ and $RE_4M_2CdGe_4$ [a]

compound	La	Ce	Pr	Nd	Sm	Gd	Tb	Dy	Ho	Er	Tm	Lu
$RE_4Mn_2AgGe_4$	+	+	+	+	+	+	+	+	+	–	–	–
$RE_4Fe_2AgGe_4$	–	+	+	+	+	+	+	+	+	+	+	+
$RE_4Co_2AgGe_4$	–	–	+	+	+	+	+	+	+	+	+	–
$RE_4Ni_2AgGe_4$	–	–	+	+	+	+	+	+	+	–	–	–
$RE_4Mn_2CdGe_4$	+	+	+	+	+	+	+	+	+	+	+	+
$RE_4Fe_2CdGe_4$	–	–	–	+	+	+	+	+	+	+	+	+
$RE_4Co_2CdGe_4$	–	+	+	+	+	+	+	+	+	+	+	–
$RE_4Ni_2CdGe_4$	–	–	–	–	+	+	+	+	+	+	–	–

[a] Legend: formed (+), unknown (–).

Table 2. Cell Parameters for RE_4M_2XGe$_4$ Refined from Powder XRD Data

compound	a (Å)	b (Å)	c (Å)	β (°)	V (Å^3)
***RE*$_4$Mn$_2$AgGe$_4$**					
La$_4$Mn$_2$AgGe$_4$	16.561(6)	4.560(2)	7.489(2)	106.204(7)	543.1(6)
Ce$_4$Mn$_2$AgGe$_4$	16.366(6)	4.356(2)	7.347(1)	106.63(2)	501.9(6)
Pr$_4$Mn$_2$AgGe$_4$	16.378(2)	4.347(1)	7.339(2)	106.73(1)	500.4(4)
Nd$_4$Mn$_2$AgGe$_4$	16.307(3)	4.326(3)	7.301(2)	106.62(3)	493.5(6)
Sm$_4$Mn$_2$AgGe$_4$	16.138(2)	4.278(1)	7.2221(6)	106.46(1)	478.2(3)
Gd$_4$Mn$_2$AgGe$_4$	15.983(2)	4.236(2)	7.110(1)	106.31(1)	462.0(4)
Tb$_4$Mn$_2$AgGe$_4$	15.937(2)	4.230(2)	7.1158(10)	106.05(1)	461.0(4)
Dy$_4$Mn$_2$AgGe$_4$	15.806(9)	4.187(6)	7.070(7)	106.17(8)	449.4(9)
Ho$_4$Mn$_2$AgGe$_4$	15.590(4)	4.169(1)	7.231(1)	108.58(2)	445.8(4)
***RE*$_4$Fe$_2$AgGe$_4$**					
Ce$_4$Fe$_2$AgGe$_4$	16.089(4)	4.191(1)	7.249(1)	106.81(2)	467.9(4)
Pr$_4$Fe$_2$AgGe$_4$	15.976(5)	4.170(2)	7.2141(8)	106.77(3)	460.2(5)
Nd$_4$Fe$_2$AgGe$_4$	15.595(3)	4.1894(8)	7.085(1)	106.17(2)	444.6(3)
Sm$_4$Fe$_2$AgGe$_4$	15.595(4)	4.124(2)	7.129(3)	106.55(8)	439.5(7)
Gd$_4$Fe$_2$AgGe$_4$	15.657(3)	4.224(2)	6.863(2)	106.48(3)	435.3(4)
Tb$_4$Fe$_2$AgGe$_4$	15.356(8)	4.203(2)	7.025(4)	106.12(2)	435.6(7)
Dy$_4$Fe$_2$AgGe$_4$	15.411(8)	4.171(3)	7.039(3)	106.30(8)	433.9(9)
Ho$_4$Fe$_2$AgGe$_4$	15.377(3)	4.178(1)	7.024(1)	106.28(3)	433.2(3)
Er$_4$Fe$_2$AgGe$_4$	15.230(4)	4.232(2)	6.948(2)	107.41(3)	427.3(5)
Tm$_4$Fe$_2$AgGe$_4$	15.181(4)	4.219(2)	6.909(2)	107.90(5)	421.1(6)
Lu$_4$Fe$_2$AgGe$_4$	15.106(6)	4.183(3)	6.849(4)	108.34(5)	410.8(8)
***RE*$_4$Co$_2$AgGe$_4$**					
Pr$_4$Co$_2$AgGe$_4$	16.124(5)	4.151(2)	7.346(2)	106.23(3)	472.1(5)
Nd$_4$Co$_2$AgGe$_4$	15.878(9)	4.252(3)	7.155(3)	106.45(2)	463.2(8)
Sm$_4$Co$_2$AgGe$_4$	14.841(5)	4.256(3)	7.17(1)	106.14(5)	435.0(9)
Gd$_4$Co$_2$AgGe$_4$	14.79(2)	4.306(6)	7.137(3)	108.50(2)	431.1(9)
Tb$_4$Co$_2$AgGe$_4$	14.578(3)	4.311(1)	7.193(3)	108.148(9)	429.5(4)
Dy$_4$Co$_2$AgGe$_4$	14.706(5)	4.179(2)	7.225(5)	108.39(2)	421.3(7)
Ho$_4$Co$_2$AgGe$_4$	14.601(4)	4.176(1)	7.1087(9)	108.13(2)	411.9(3)

$Er_4Co_2AgGe_4$	14.410(7)	4.160(1)	6.972(3)	108.80(3)	395.6(5)
$Tm_4Co_2AgGe_4$	14.228(4)	4.150(8)	6.817(2)	107.21(3)	384.5(9)
***RE*$_4$Ni$_2$AgGe$_4$**					
$Pr_4Ni_2AgGe_4$	16.271(5)	4.330(4)	7.181(5)	108.30(4)	480.3(9)
$Nd_4Ni_2AgGe_4$	16.01(1)	4.070(5)	7.346(4)	108.11(5)	454.9(9)
$Sm_4Ni_2AgGe_4$	15.605(3)	4.123(2)	7.215(4)	108.01(4)	441.5(7)
$Gd_4Ni_2AgGe_4$	15.243(8)	4.103(3)	7.238(3)	107.97(4)	430.6(8)
$Tb_4Ni_2AgGe_4$	15.138(4)	4.089(2)	7.252(2)	107.78(3)	427.5(5)
$Dy_4Ni_2AgGe_4$	14.874(4)	4.021(2)	6.947(9)	107.11(4)	397.1(9)
$Ho_4Ni_2AgGe_4$	14.819(4)	4.015(2)	6.916(2)	108.25(3)	390.8(5)
***RE*$_4$Mn$_2$CdGe$_4$**					
$La_4Mn_2CdGe_4$	16.732(4)	4.403(2)	7.539(2)	107.16(2)	530.7(6)
$Ce_4Mn_2CdGe_4$	16.508(4)	4.353(1)	7.448(1)	107.13(2)	511.5(4)
$Pr_4Mn_2Cd_2Ge_4$	16.467(2)	4.340(2)	7.412(2)	106.78(2)	507.2(5)
$Nd_4Mn_2CdGe_4$	16.372(4)	4.314(3)	7.382(3)	107.04(6)	498.5(8)
$Sm_4Mn_2CdGe_4$	16.142(5)	4.243(2)	7.251(2)	106.61(1)	475.9(6)
$Gd_4Mn_2CdGe_4$	16.110(7)	4.246(5)	7.237(2)	106.36(4)	475.0(9)
$Tb_4Mn_2CdGe_4$	16.034(8)	4.267(3)	7.186(4)	106.08(2)	472.4(9)
$Dy_4Mn_2CdGe_4$	15.775(7)	4.156(2)	7.079(2)	106.22(2)	445.6(6)
$Ho_4Mn_2CdGe_4$	15.817(4)	4.141(1)	7.089(2)	106.106(6)	446.1(4)
$Er_4Mn_2CdGe_4$	15.746(5)	4.120(2)	7.048(2)	106.081(8)	439.3(5)
$Tm_4Mn_2CdGe_4$	15.670(4)	4.112(2)	7.022(2)	106.06(2)	434.8(5)
$Lu_4Mn_2CdGe_4$	15.586(3)	4.074(1)	6.975(2)	105.799(6)	426.2(3)
***RE*$_4$Fe$_2$CdGe$_4$**					
$Nd_4Fe_2CdGe_4$	16.168(2)	4.333(1)	7.292(2)	107.31(1)	487.7(4)
$Sm_4Fe_2CdGe_4$	15.793(9)	4.242(3)	7.153(4)	107.34(3)	457.4(9)
$Gd_4Fe_2CdGe_4$	15.691(6)	4.207(2)	7.081(3)	107.102(7)	446.8(6)
$Tb_4Fe_2CdGe_4$	15.645(6)	4.202(3)	7.061(4)	107.18(4)	443.5(9)
$Dy_4Fe_2CdGe_4$	15.60(2)	4.179(5)	7.047(7)	107.15(2)	439.0(9)
$Ho_4Fe_2CdGe_4$	15.50(2)	4.148(6)	6.96(1)	107.25(2)	427.4(9)
$Er_4Fe_2CdGe_4$	15.478(6)	4.143(2)	6.966(3)	107.058(8)	427.0(6)
$Tm_4Fe_2CdGe_4$	15.392(9)	4.123(2)	6.924(4)	107.052(5)	420.1(7)

$Lu_4Fe_2CdGe_4$	15.290(5)	4.092(3)	6.882(3)	106.86(1)	412.1(7)
***RE*$_4$Co$_2$CdGe$_4$**					
$Ce_4Co_2CdGe_4$	15.993(8)	4.306(3)	7.274(4)	107.33(1)	478.1(9)
$Pr_4Co_2CdGe_4$	15.862(2)	4.292(1)	7.231(1)	107.51(1)	469.5(3)
$Nd_4Co_2CdGe_4$	15.778(2)	4.272(1)	7.2031(6)	107.42(4)	463.2(3)
$Sm_4Co_2CdGe_4$	15.671(2)	4.237(2)	7.108(3)	107.41(2)	450.3(5)
$Gd_4Co_2CdGe_4$	15.587(5)	4.203(3)	7.053(2)	107.32(2)	441.1(8)
$Tb_4Co_2CdGe_4$	15.586(9)	4.202(3)	7.053(5)	107.38(3)	440.8(9)
$Dy_4Co_2CdGe_4$	15.436(3)	4.177(2)	6.987(1)	107.42(2)	429.8(4)
$Ho_4Co_2CdGe_4$	15.375(2)	4.158(2)	6.956(1)	107.42(2)	424.3(4)
$Er_4Co_2CdGe_4$	15.304(2)	4.1418(9)	6.9278(8)	107.43(2)	419.0(3)
$Tm_4Co_2CdGe_4$	15.229(2)	4.123(2)	6.8896(9)	107.38(2)	412.8(4)
***RE*$_4$Ni$_2$CdGe$_4$**					
$Sm_4Ni_2CdGe_4$	15.708(3)	4.227(1)	7.111(1)	108.39(1)	448.0(3)
$Gd_4Ni_2CdGe_4$	15.593(3)	4.2154(7)	7.081(2)	108.21(2)	442.1(4)
$Tb_4Ni_2CdGe_4$	15.521(2)	4.1915(8)	7.028(1)	108.29(1)	434.1(2)
$Dy_4Ni_2CdGe_4$	15.366(10)	4.164(4)	6.966(5)	108.10(4)	423.7(9)
$Ho_4Ni_2CdGe_4$	15.373(6)	4.162(1)	6.966(2)	108.23(2)	423.3(5)
$Er_4Ni_2CdGe_4$	15.281(4)	4.155(2)	6.945(2)	108.18(2)	418.9(5)

Table 3. Crystallographic Data for $Nd_4Mn_2AgGe_4$ and $Nd_4Mn_2Cd(Ge_{1-y}Si_y)_4$ [a]

	$Nd_4Mn_{1.55(2)}Ag_{1.25(2)}Ge_4$	$Nd_4Mn_2Cd_{0.86(1)}Ge_4$	$Nd_4Mn_2Cd_{0.92(1)}Ge_{2.22(1)}Si_{1.78(1)}$	$Nd_4Mn_2Cd_{0.98(1)}Ge_{1.46(3)}Si_{2.54(3)}$	$Nd_4Mn_2Cd_{0.97(1)}Si_4$
fw (amu)	1087.31	1073.86	1001.40	976.12	908.79
a (Å)	16.281(5)	16.016(2)	16.224(12)	16.182(2)	16.0991(10)
b (Å)	4.3473(12)	4.2263(5)	4.305(3)	4.2870(5)	4.2746(3)
c (Å)	7.319(2)	7.1880(9)	7.305(5)	7.2859(9)	7.2517(5)
β (°)	106.855(4)	106.4057(18)	107.023(10)	107.1243(17)	107.2161(10)
V (Å^3)	495.8(2)	466.74(10)	487.9(6)	483.02(10)	476.68(6)
ρ_c (g cm^{-3})	7.284	7.641	6.816	6.712	6.332
μ (mm^{-1})	36.69	38.92	32.20	30.44	26.49
$R(F)$ [b]	0.038	0.036	0.021	0.042	0.020
$R_w(F_o^2)$ [c]	0.091	0.099	0.041	0.127	0.035

[a] For all structures, space group $C2/m$ (No. 12), $Z = 2$, $T = 296(2)$ K, $\lambda = 0.71073$ Å. [b] $R(F) = \sum||F_o| - |F_c|| / \sum|F_o|$ for $F_o^2 > 2\sigma(F_o^2)$. [c] $R_w(F_o^2) = [\sum[w(F_o^2 - F_c^2)^2] / \sum wF_o^4]^{1/2}$; $w^{-1} = [\sigma^2(F_o^2) + (Ap)^2 + Bp]$, where $p = [\max(F_o^2,0) + 2F_c^2] / 3$.

Table 4. Ranges of Interatomic Distances (Å) for $Nd_4Mn_2AgGe_4$ and $Nd_4Mn_2Cd(Ge_{1-y}Si_y)_4$

compound	$Nd_4Mn_{1.55(2)}Ag_{1.25(2)}Ge_4$	$Nd_4Mn_2Cd_{0.86(1)}Ge_4$	$Nd_4Mn_2Cd_{0.92(1)}Ge_{2.22(1)}Si_{1.78(1)}$	$Nd_4Mn_2Cd_{0.98(1)}Ge_{1.46(3)}Si_{2.54(3)}$	$Nd_4Mn_2Cd_{0.97(1)}Si_4$
*RE*1–*Tt*	3.018(1)–3.116(2)	2.961(1)–3.042(1)	3.022(2)–3.123(2)	3.021(2)–3.121(2)	3.022(1)–3.129(1)
*RE*1–*M*	3.371(2)–3.506(1)	3.333(2)–3.432(2)	3.349(2)–3.485(2)	3.339(2)–3.472(2)	3.318(1)–3.460(1)
*RE*1–*X*	3.427(1)	3.399(1)	3.437(2)	3.426(1)	3.412(1)
*RE*2–*Tt*	3.122(1)–3.152(1)	3.020(1)–3.094(1)	3.066(2)–3.145(2)	3.045(2)–3.139(2)	3.022(1)–3.132(1)
*RE*2–*M*	3.247(2)–3.276(1)	3.178(2)–3.221(2)	3.224(3)–3.234(2)	3.213(2)–3.218(2)	3.192(1)–3.195(1)
*RE*2–*X*	3.410(1)	3.348(1)	3.409(2)	3.398(1)	3.386(1)
M–*Tt*	2.621(1)–2.692(2)	2.573(1)–2.607(2)	2.575(2)–2.625(2)	2.556(2)–2.606(3)	2.528(1)–2.568(2)
X–*Tt*	2.958(1)–3.166(2)	2.930(1)–3.099(2)	2.990(2)–3.196(2)	2.999(3)–3.206(2)	3.002(2)–3.223(2)
Tt–*Tt*	2.548(3)	2.553(3)	2.515(2)	2.479(5)	2.433(3)

Table 5. –ICOHP values for $La_4Mn_2AgGe_4$ and $La_4Cd_2AgGe_4$

contact	–ICOHP (eV bond^{-1})	–ICOHP (eV cell^{-1})	contribution (%)
$La_4Mn_2AgGe_4$			
La–Ge	0.95	10.43	42.2
Mn–Ge	2.19	8.75	35.4
Ag–Ge	0.85	3.40	13.8
Ge–Ge	2.12	2.12	8.6
$La_4Mn_2CdGe_4$			
La–Ge	0.94	10.33	42.0
Mn–Ge	2.25	9.01	36.6
Cd–Ge	0.80	3.21	13.0
Ge–Ge	2.07	2.07	8.4

Figure Captions

Figure 1. Plots of unit cell volumes for (a) $RE_4M_2AgGe_4$ and (b) $RE_4M_2CdGe_4$ (M = Mn–Ni).

Figure 2. Structure map for $RE_4M_2AgGe_4$ and $RE_4M_2CdGe_4$ based on ratios of Pauling metallic radii (green circles are known phases; red crosses are unknown phases).

Figure 3. Structure of $RE_4M_2XGe_4$ (M = Mn–Ni; X = Ag, Cd). (a) Ge-centred trigonal prisms and X-centred tetragonal prisms. (b) Covalent [M_2XGe_4] framework with RE atoms situated within tunnels. (c) Ladders of edge-sharing M-centred tetrahedra and stacks of X-centred cuboctahedra.

Figure 4. Plots of (a) selected cell parameters, (b) site occupancies, and (c) interatomic distances as a function of nominal Si content in the solid solution $Nd_4Mn_2Cd(Ge_{1-y}Si_y)_4$. (d) As the Si content increases, the $Tt1$–$Tt1$ pair shortens while the $CdTt_4$ square plane expands.

Figure 5. Density of states (DOS) and crystal orbital Hamilton population (COHP) curves for (a) $La_4Mn_2AgGe_4$ and (b) $La_4Mn_2CdGe_4$.

Figure 6. Thermal properties for $Nd_4Mn_2InGe_4$ and $Nd_4Mn_2AgGe_4$.

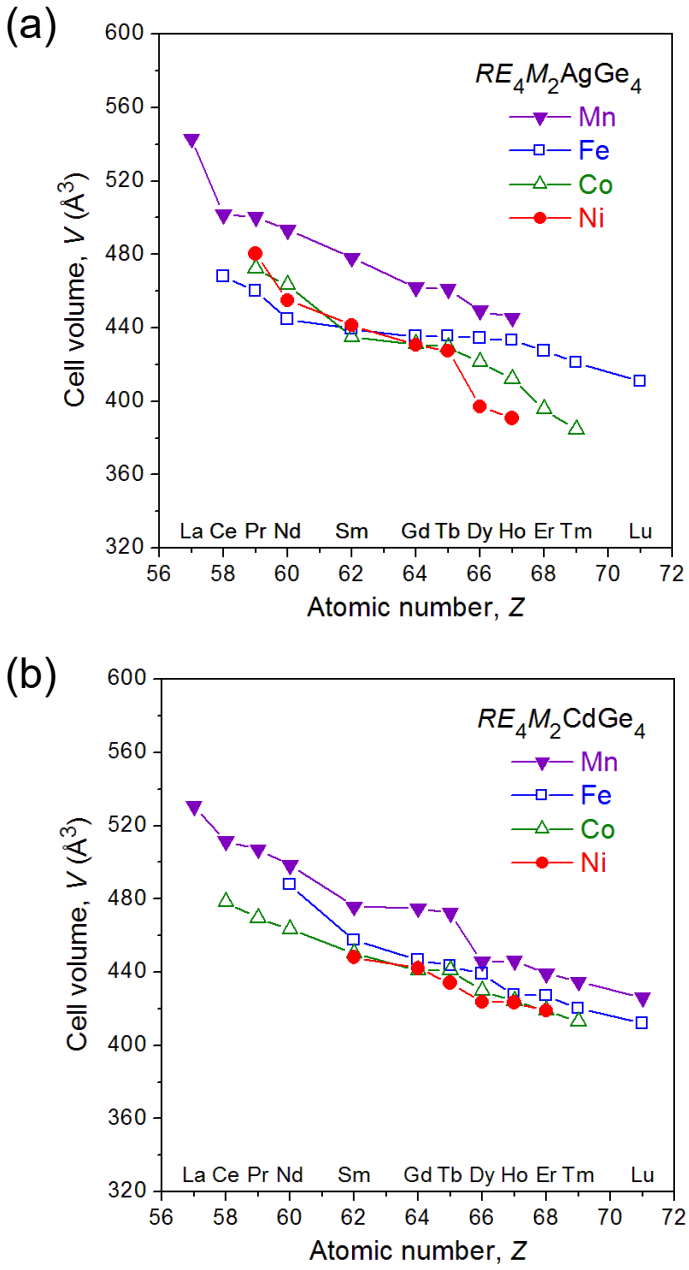

Figure 1. Plots of unit cell volumes for (a) $RE_4M_2AgGe_4$ and (b) $RE_4M_2CdGe_4$ (M = Mn–Ni).

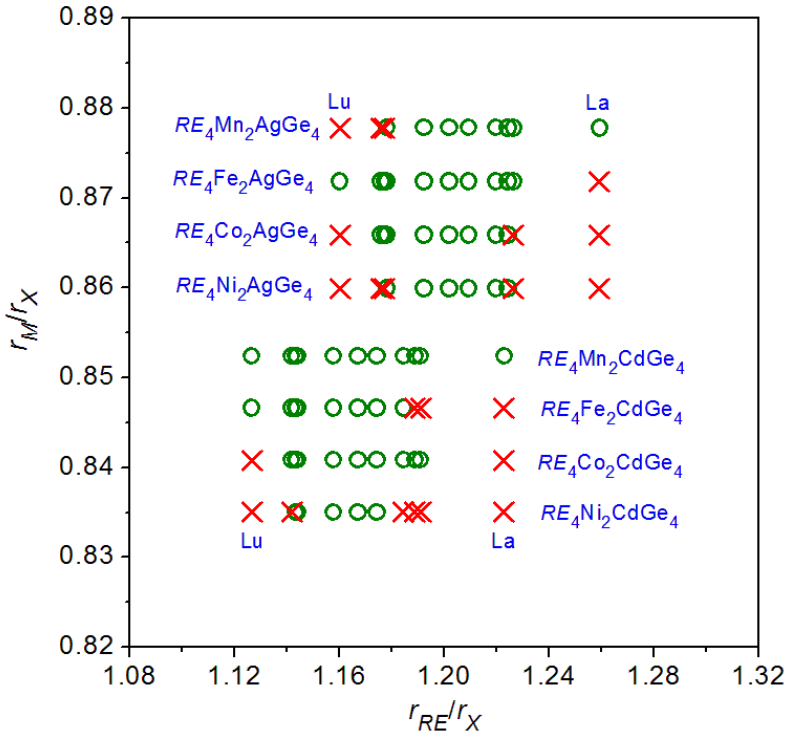

Figure 2. Structure map for $RE_4M_2AgGe_4$ and $RE_4M_2CdGe_4$ based on ratios of Pauling metallic radii (green circles are known phases; red crosses are unknown phases).

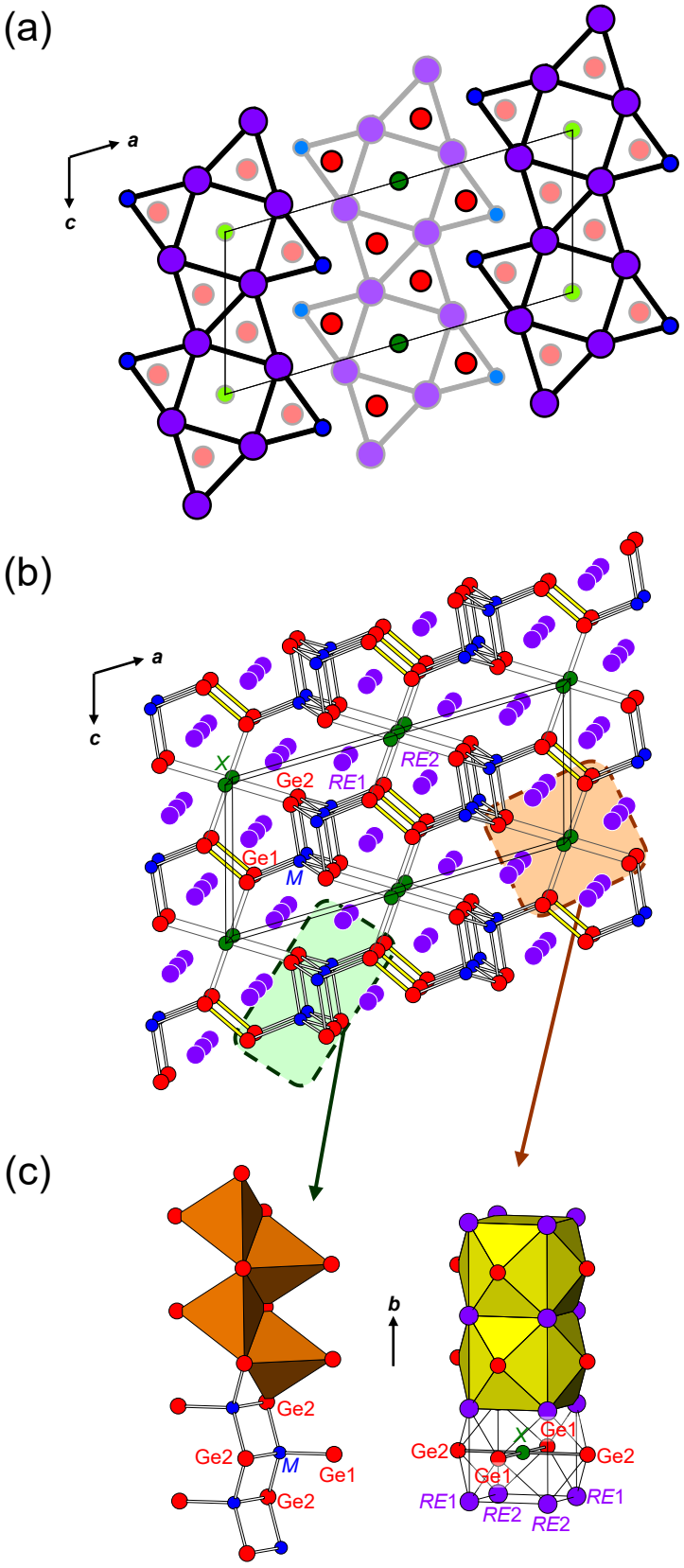

Figure 3. Structure of $RE_4M_2X\mathrm{Ge}_4$ (M = Mn–Ni; X = Ag, Cd). (a) Ge-centred trigonal prisms and X-centred tetragonal prisms. (b) Covalent $[M_2X\mathrm{Ge}_4]$ framework with RE atoms situated within tunnels. (c) Ladders of edge-sharing M-centred tetrahedra and stacks of X-centred cuboctahedra.

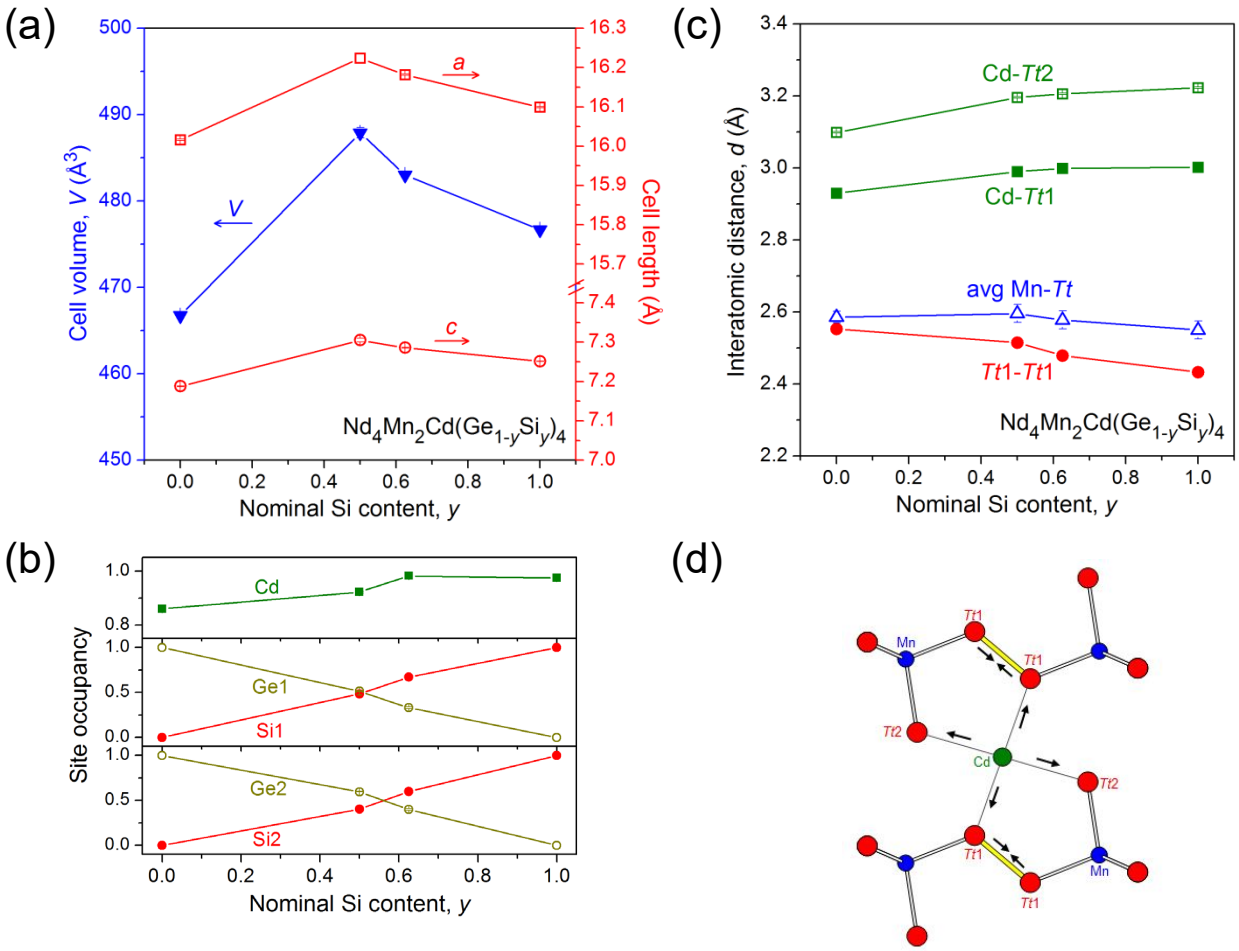

Figure 4. Plots of (a) selected cell parameters, (b) site occupancies, and (c) interatomic distances as a function of nominal Si content in the solid solution $Nd_4Mn_2Cd(Ge_{1-y}Si_y)_4$. (d) As the Si content increases, the *Tt*1–*Tt*1 pair shortens while the Cd*Tt*$_4$ square plane expands.

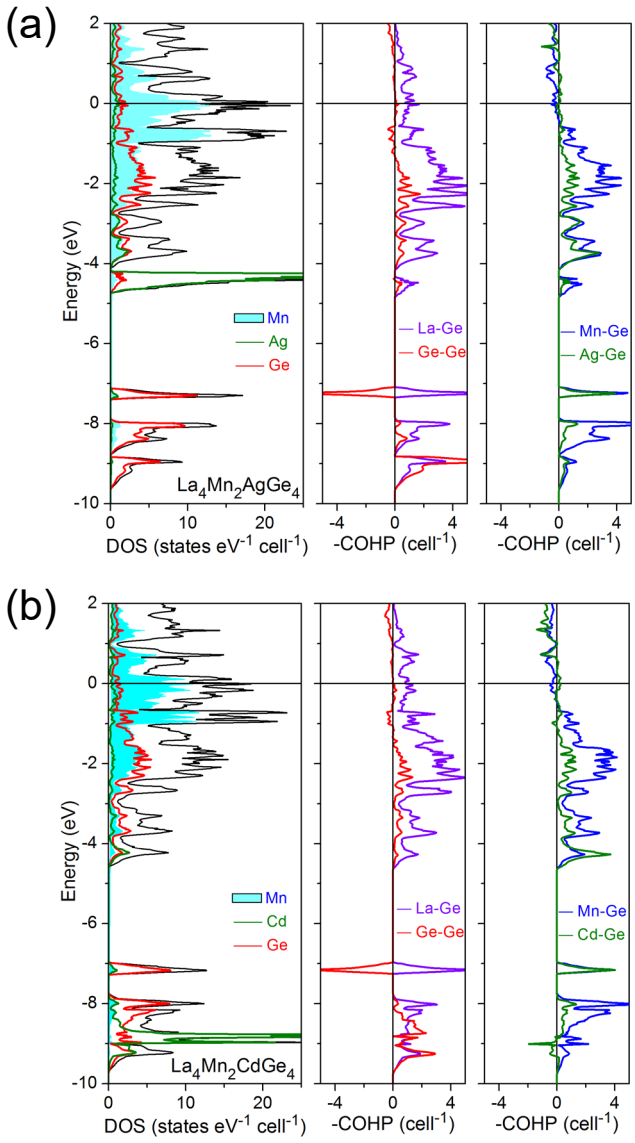

Figure 5. Density of states (DOS) and crystal orbital Hamilton population (COHP) curves for (a) $La_4Mn_2AgGe_4$ and (b) $La_4Mn_2CdGe_4$.

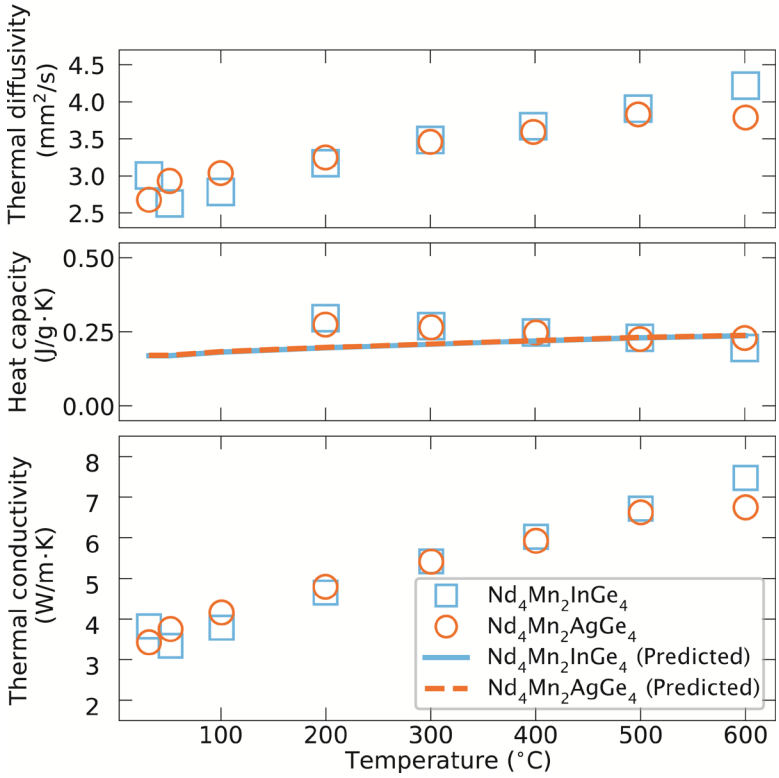

Figure 6. Thermal properties for $Nd_4Mn_2InGe_4$ and $Nd_4Mn_2AgGe_4$.

Associated Content

Supporting Information

The Supporting Information is available free of charge on the ACS Publications website at DOI: 10.1021/acs.inorgchem.xxxxxxx.

Phase analysis of samples; full crystallographic data; representative XRD and SEM analyses (PDF).

Accession Codes

CCDC 1860760–1860764 contain the supplementary crystallographic data for this paper. These data can be obtained free of charge via www.ccdc.cam.ac.uk/data_request/cif, or by emailing data_request@ccdc.cam.ac.uk, or by contacting The Cambridge Crystallographic Data Centre, 12 Union Road, Cambridge CB2 1EZ, UK; fax: +44 1223 336033.

Author Information

Corresponding Authors

* E-mail: oliynyk@ualberta.ca (A.O.O.).

* E-mail: sparks@eng.utah.edu (T.D.S.).

* E-mail: arthur.mar@ualberta.ca (A.M.).

ORCID

Anton O. Oliynyk: 0000-0003-0732-7340

Taylor D. Sparks: 0000-0001-8020-7711

Arthur Mar: 0000-0003-0474-5918

Notes

The authors declare no competing financial interest.

Acknowledgments

This work was supported by the Canada First Research Excellence Fund (CFREF, through the Future Energy Systems Research Institute at the University of Alberta, Project T12-P01), the Natural Sciences and Engineering Research Council of Canada (NSERC, through Discovery Grant RGPIN-2018-04294), the NSERC Collaborative Research and Training Experience Program (CREATE, through the Alberta/Technical University of Munich International Graduate School), the University of Alberta Research Experience program (UARE, through Solid State Inorganic Chemistry project), and the National Science Foundation (NSF, through CAREER award DMR 1651668).

References

(1) Salamakha, P. S. Crystal structures and crystal chemistry of ternary rare-earth germanides. In *Handbook on the Physics and Chemistry of Rare Earths*; Gschneidner, K. A., Jr., Eyring, L., Eds.; Elsevier: Amsterdam, 1999; Vol. 27, pp 225–338.

(2) Chen, J.; Semeniuk, K.; Feng, Z.; Reiss, P.; Brown, P.; Zou, Y.; Logg, P. W.; Lampronti, G. I.; Grosche, F. M. Unconventional superconductivity in the layered iron germanide YFe_2Ge_2. *Phys. Rev. Lett.* **2016**, *116*, 127001-1–127001-5.

(3) Chajewski, G.; Samsel-Czekała, M.; Hackemer, A.; Wiśniewski, P.; Pikul, A. P.; Kaczorowski, D. Superconductivity in YTE_2Ge_2 compounds (*TE* = d-electron transition metal). *Physica B* **2018**, *536*, 767–772.

(4) Sing, Y.; Ramakrishnan, S. Magnetic ordering and superconductivity in the $R_2Ir_3Ge_5$ (*R* = Y, La, Ce–Nd, Gd–Tm, Lu) system. *Phys. Rev. B* **2004**, *69*, 174423-1–174423-13.

(5) Pecharsky, V. K.; Gschneidner, K. A. Jr. Giant magnetocaloric effect in $Gd_5(Si_2Ge_2)$. *Phys. Rev. Lett.* **1997**, *78*, 4494–4497.

(6) Steurer, W.; Dshemuchadse, J. *Intermetallics: Structures, Properties, and Statistics*; Oxford University Press: Oxford, 2016.

(7) Wu, X.; Kanatzidis, M. G. *RE*$AuAl_4Ge_2$ and *RE*$AuAl_4(Au_xGe_{1-x})_2$ (*RE* = rare earth element): Quaternary intermetallics grown in liquid aluminum. *J. Solid State Chem.* **2005**, *178*, 3233–3242.

(8) He, W.; Zeng, W.; Lin, G. Crystal structures of new $R_3CoAl_3Ge_2$ (R = Gd–Er) quaternary compounds and magnetic properties and lattice thermal expansion of $Gd_3CoAl_3Ge_2$. *J. Alloys Compd.* **2015**, *627*, 307–312.

(9) Zhuravleva, M. A.; Pcionek, R. J.; Wang, X.; Schultz, A. J.; Kanatzidis, M. G. $REMGa_3Ge$ and $RE_3Ni_3Ga_8Ge_3$ (M = Ni, Co; RE = rare-earth element): New intermetallics synthesized in liquid gallium. X-ray, electron, and neutron structure determination and magnetism. *Inorg. Chem.* **2003**, *42*, 6412–6424.

(10) Zhuravleva, M. A.; Kanatzidis, M. G. Polygallide $RE_2MGa_9Ge_2$ (RE = Ce, Sm; M = Ni, Co) phases grown in molten gallium. *Inorg. Chem.* **2008**, *47*, 9471–9477.

(11) Subbarao, U.; Jana, R.; Chondroudi, M.; Balasubramanian, M.; Kanatzidis, M. G.; Peter, S. C. $Yb_7Ni_4InGe_{12}$: a quaternary compound having mixed valent Yb atoms grown from indium flux. *Dalton Trans.* **2015**, *44*, 5797–5804.

(12) Chondroudi, M.; Peter, S. C.; Malliakas, C. D.; Balasubramanian, M.; Li, Q.; Kanatzidis, M. G. $Yb_3AuGe_2In_3$: An ordered variant of the YbAuIn structure exhibiting mixed-valent Yb behavior. *Inorg. Chem.* **2011**, *50*, 1184–1193.

(13) Salvador, J. R.; Kanatzidis, M. G. Indium flux synthesis of $RE_4Ni_2InGe_4$ (RE = Dy, Ho, Er, and Tm): An ordered quaternary variation on the binary phase Mg_5Si_6. *Inorg. Chem.* **2006**, *45*, 7091–7099.

(14) Oliynyk, A. O.; Stoyko, S. S.; Mar, A. Quaternary germanides $RE_4Mn_2InGe_4$ (RE = La–Nd, Sm, Gd–Tm, Lu). *Inorg. Chem.* **2013**, *52*, 8264–8271.

(15) Oliynyk, A. O.; Stoyko, S. S.; Mar, A. Many metals make the cut: Quaternary rare-earth germanides $RE_4M_2InGe_4$ (M = Fe, Co, Ni, Ru, Rh, Ir) and $RE_4RhInGe_4$ derived from excision of slabs in RE_2InGe_2. *Inorg. Chem.* **2015**, *54*, 2780–2792.

(16) Oliynyk, A. O.; Djama-Kayad, K.; Mar, A. Investigation of phase equilibria in the quaternary Ce–Mn–In–Ge system and isothermal sections of the boundary ternary systems at 800 °C. *J. Alloys Compd.* **2015**, *622*, 837–841.

(17) Tobash, P. H.; Lins, D.; Bobev, S.; Lima, A.; Hundley, M. F.; Thompson, J. D.; Sarrao, J. L. Crystal growth, structural, and property studies on a family of ternary rare-earth phases RE_2InGe_2 (RE = Sm, Gd, Tb, Dy, Ho, Yb). *Chem. Mater.* **2005**, *17*, 5567–5573.

(18) Graf, T.; Felser, C.; Parkin, S. S. P. Simple rules for the understanding of Heusler compounds. *Prog. Solid State Chem.* **2011**, *39*, 1–50.

(19) Sales, B. C.; May, A. F.; McGuire, M. A.; Stone, M. B.; Singh, D. J.; Mandrus, D. Transport, thermal, and magnetic properties of the narrow-gap semiconductor $CrSb_2$. *Phys. Rev. B* **2012**, *86*, 235136-1–235136-7.

(20) Calta, N. P.; Im, J.; Rodriguez, A. P.; Fang, L.; Bulgaris, D. E.; Chasapis, T. C.; Freeman, A. J.; Kanatzidis, M. G. Hybridization gap and Dresselhaus spin splitting in $EuIr_4In_2Ge_4$. *Angew. Chem. Int. Ed.* **2015**, *54*, 9186–9191.

(21) Calta, N. P.; Im, J.; Fang, L.; Chasapis, T. C.; Bulgaris, D. E.; Chung, D. Y.; Kwok, W.-K.; Kanatzidis, M. G. Hybridization gap in the semiconducting compound $SrIr_4In_2Ge_4$. *Inorg. Chem.* **2016**, *55*, 12477–12481.

(22) Oliynyk, A. O.; Mar, A. Discovery of intermetallic compunds from traditional to machine-learning approaches. *Acc. Chem. Res.* **2018**, *51*, 59–68.

(23) Graser, J.; Kauwe, S. K.; Sparks, T. D. Machine learning and energy minimization approaches for crystal structure predictions: A review and new horizons. *Chem. Mater.* **2018**, *30*, 3601–3612.

(24) Sparks, T. D.; Gaultois, M. W.; Oliynyk, A.; Brgoch, J.; Meredig, B. Data mining our way to the next generation of thermoelectrics. *Scr. Mater.* **2016**, *111*, 10–15.

(25) Gaultois, M. W.; Oliynyk, A. O.; Mar, A.; Sparks, T. D.; Mulholland, G. J.; Meredig, B. Perspective: Web-based machine learning models for real-time screening of thermoelectric

materials properties. *APL Mater.* **2016**, *4*, 053213-1–053213-11. For the implementation of these tools, see *http://thermoelectrics.citrination.com*.

(26) Oliynyk, A. O.; Sparks, T. D.; Gaultois, M. W.; Ghadbeigi, L.; Mar, A. $Gd_{12}Co_{5.3}Bi$ and $Gd_{12}Co_5Bi$, crystalline Doppelgänger with low thermal conductivities. *Inorg. Chem.* **2016**, *55*, 6625–6633.

(27) Kauwe, S. K.; Graser, J.; Vazquez, A.; Sparks, T. D. Machine learning prediction of heat capacity for solid inorganics. *Integr. Mater. Manuf. Innov.* **2018**, *7*, 43–51.

(28) Xue, D.; Balachandran, P. V.; Hogden, J.; Theiler, J.; Xue, D.; Lookman, T. Accelerated search for materials with targeted properties by adaptive design. *Nat. Commun.* **2016**, *7*, 11241-1–11241-9.

(29) Balachandran, P. V.; Kowalski, B.; Sehirlioglu, A.; Lookman, T. Experimental search for high-temperature ferroelectric perovskites guided by two-step machine learning. *Nat. Commun.* **2018**, *9*, 1668-1–1668-9.

(30) Zhuo, Y.; Mansouri Tehrani, A.; Brgoch, J. Predicting the band gaps of inorganic solids by machine learning. *J. Phys. Chem. Lett.* **2018**, *9*, 1668–1673.

(31) Oliynyk, A. O.; Gaultois, M. W.; Hermus, M.; Morris, A. J.; Mar, A.; Brgoch, J. Searching for missing binary equiatomic phases: Complex crystal chemistry in the Hf–In system. *Inorg. Chem.* **2018**, *57*, 7966–7974.

(32) Cao, B.; Adutwum, L. A.; Oliynyk, A. O.; Luber, E. J.; Olsen, B. C.; Mar, A.; Buriak, J. M. How to optimize materials and devices *via* design of experiments and machine learning: Demonstration using organic photovoltaics. *ACS Nano* **2018**, *12*, 7434–7444.

(33) Mansouri Tehrani, A.; Oliynyk, A. O.; Parry, M.; Rizvi, Z.; Couper, S.; Lin, F.; Miyagi, L.; Sparks, T. D.; Brgoch, J. Machine learning directed search for ultraincompressible, superhard materials. *J. Am. Chem. Soc.* **2018**, *140*, 9844–9853.

(34) Akselrud, L.; Grin, Yu. *WinCSD*: Software package for crystallographic calculations (Version 4). *J. Appl. Crystallogr.* **2014**, *47*, 803–805.

(35) Sheldrick, G. M. *SHELXTL*, version 6.12; Bruker AXS Inc.: Madison, WI, 2001.

(36) Gelato, L. M.; Parthé, E. *STRUCTURE TIDY* – a computer program to standardize crystal structure data. *J. Appl. Crystallogr.* **1987**, *20*, 139–143.

(37) Spek, A. L. Structure validation in chemical crystallograpy. *Acta Crystallogr., Sect. D* **2009**, *65*, 148–155.

(38) Tank, R.; Jepsen, O.; Burkhardt, A.; Andersen, O. K. *TB-LMTO-ASA Program*, version 4.7; Max Planck Institut für Festkörperforschung: Stuttgart, Germany, 1998.

(39) Dronskowski, R.; Blöchl, P. E. Crystal orbital Hamilton populations (COHP). Energy-resolved visualization of chemical bonding in solids based on density-functional calculations. *J. Phys. Chem.* **1993**, *97*, 8617–8624.

(40) Cape, J. A.; Lehman, G. W. Temperature and finite pulse-time effects in the flash method for measuring thermal diffusivity. *J. Appl. Phys.* **1963**, *34*, 1909–1913.

(41) Pauling, L. *The Nature of the Chemical Bond*, 3rd ed.; Cornell University Press: Ithaca, NY, 1960.

(42) Guo, S. P.; Meyers, J. J.; Tobash, P. H.; Bobev, S. Eleven new compounds in the RE–Cd–Ge systems (RE = Pr, Nd, Sm, Gd–Yb; Y): Crystal chemistry of the RE_2CdGe_2 series. *J. Solid State Chem.* **2012**, *192*, 16–32.

(43) Young, A. G.; Hanton, L. R. Square planar silver(I) complexes: A rare but increasingly observed stereochemistry for silver(I). *Coord. Chem. Rev.* **2008**, *252*, 1346–1386.

(44) *Pearson's Crystal Data: Crystal Structure Database for Inorganic Compounds (on DVD)*, release 2015/16; ASM International: Materials Park, OH, 2016.

(45) Bażela, W.; Szytuła, A.; Todorović, J.; Zięba, A. Crystal and magnetic structure of the $NiMnGe_{1-n}Si_n$ system. *Phys. Status Solidi A* **1981**, *64*, 367–378.

(46) Cordruwisch, E.; Kaczorowski, D.; Saccone, A.; Rogl, P.; Ferro, R. Constitution, structural chemistry, and magnetism of the ternary system Ce–Ag–Ge. *J. Phase Equilib.* **1999**, *20*, 407–422.

(47) Castellanos, M.; West, A. R. Deviations from Vegard's law in oxide solid solutions. *J. Chem. Soc., Faraday Trans. 1* **1980**, *76*, 2159–2169.

(48) Terada, Y.; Okhubo, K.; Mohri, T.; Suzuki, T. Thermal conductivity of intermetallic compounds with metallic bonding. *Mater. Trans.* **2002**, *43*, 3167–3176.

For Table of Contents Only

Germanides $RE_2M_2X\mathrm{Ge}_4$ as well as the solid solution $\mathrm{Nd}_4\mathrm{Mn}_2\mathrm{Cd}(\mathrm{Ge}_{1-y}\mathrm{Si}_y)_4$ adopt monoclinic structures containing *X* atoms encapsulated within large cages. They serve as a test case to validate machine-learning models which predict low thermal conductivities for these intermetallic compounds.